CrossMark

J. Fluid Mech. (2018), *vol.* 846, *pp.* 482–507. © Cambridge University Press 2018
doi:10.1017/jfm.2018.242

Turbulent drag reduction in plane Couette flow with polymer additives: a direct numerical simulation study

Hao Teng[1], **Nansheng Liu**[1,†], **Xiyun Lu**[1] **and Bamin Khomami**[2,†]

[1]Department of Modern Mechanics, University of Science and Technology of China, Hefei, Anhui 230026, China

[2]Department of Chemical and Biomolecular Engineering, University of Tennessee, Knoxville, TN 37996, USA

(Received 6 November 2017; revised 6 February 2018; accepted 14 March 2018; first published online 8 May 2018)

Drag reduction (DR) in plane Couette flow (PCF) induced by the addition of flexible polymers has been studied via direct numerical simulation (DNS). The similarities and differences in the drag reduction features of PCF and plane Poiseuille flow (PPF) have been examined in detail, particularly in regard to the polymer-induced modification of large-scale structures (LSSs) in the near-wall turbulence. Specifically, it has been demonstrated that in the near-wall region, drag-reduced PCF has features similar to those of drag-reduced PPF; however, in the core region, intriguing differences are found between these two drag-reduced shear flows. Chief among these differences is the significant polymer stretch that arises from the enhanced exchanges between elastic potential energy and turbulent kinetic energy and the commensurate observation of peak values of the conformation tensor components C_{yy} and C_{zz} in this region. This finding is in stark contrast to that of drag-reduced PPF where the polymer stretch and the exchanges between elastic potential energy and turbulent kinetic energy in the core region are insignificant; to this end, in drag-reduced PPF, peak values of the conformation tensor components appear in the near-wall region. Therefore, this study paves the way for understanding the underlying flow physics in drag-reduced PCF, particularly in the context of elastic theory. Moreover, the longitudinal large-scale streaks at the channel centre of drag-reduced PCF are greatly strengthened due to the increased production/dissipation ratio; the LSS imprint effects on the near-wall flow of drag-reduced PCF monotonically increase as the Weissenberg number is enhanced.

Key words: drag reduction, polymers, turbulent flows

1. Introduction

The phenomenon of drag reduction, which occurs ubiquitously in flows of dilute polymeric solutions, has been studied extensively since it was first discovered several decades ago (Toms 1949). The study of drag reduction in viscoelastic fluids by direct numerical simulation (DNS) began approximately 20 years ago with Sureshkumar,

† Email addresses for correspondence: lns@ustc.edu.cn, bkhomami@utk.edu

https://doi.org/10.1017/jfm.2018.242 Published online by Cambridge University Press

Beris & Handler (1997). Since then, there has been much progress regarding the mechanisms of polymer-induced drag reduction and the maximum drag reduction (MDR) asymptote. Recently, Li, Sureshkumar & Khomami (2015) proposed a framework that ascribes the extent of drag reduction from its onset to MDR in wall-bounded turbulent flows to the polymer-induced change in terms of a single parameter, namely, the time scale ratio of streamwise vorticity fluctuations to vortex rotation. Specifically, MDR is achieved when these two time scales become nearly equal, hence, this underscores the important role the outer flow length scale plays in this phenomenon. This simple framework is also consistent with universal phenomena observed in polymer-induced drag-reduced flows, such as a broadened buffer layer, smaller streamwise variance, weaker streamwise vortices and larger spanwise spacing between wall streaks (e.g. Stone *et al.* 2004; White & Mungal 2008; Graham 2014).

The mechanisms for polymer-induced drag reduction are generally divided into two major theories, namely, the viscous theory and the elastic theory. According to the viscous theory proposed by Lumley (1969), polymer stretch in turbulent flow results in a substantial increase of effective viscosity in a region outside of the viscous sublayer and in the buffer layer, which suppresses turbulent fluctuations, increases the thickness of the buffer layer and reduces the wall friction. The viscous theory was recently verified in quantity by Benzi *et al.* (2004), L'vov *et al.* (2004), Benzi *et al.* (2005, 2006) and reviewed by Procaccia, L'vov & Benzi (2008). The elastic theory originally proposed by Tabor & de Gennes (1986) and actively studied in recent years (Min, Choi & Yoo 2003*a*; Min *et al.* 2003*b*; Dubief *et al.* 2004; Dallas, Vassilicos & Hewitt 2010; Thais, Gatskid & Mompeana 2012, 2013; Li *et al.* 2015) is based on the premise that the elastic energy stored by the polymer becomes comparable to the kinetic energy in the buffer layer. Since in these flows, the viscoelastic length scale is larger than the Kolmogorov scale, the usual energy cascade is inhibited, which results in buffer layer thickening and drag reduction. Min *et al.* (2003*a*) and Dallas *et al.* (2010) describe an elastic scenario in which the elastic energy stored in the near-wall region due to the uncoiling of polymer molecules is transported to and, to some extent, released in the buffer and log-law layers.

To date, much research effort has been focused on drag reduction in plane and pipe Poiseuille flows, Taylor–Couette flow and boundary layers. Although several reviews have documented the extensive research in drag-reduced shear flows, very little published work on drag reduction in plane Couette flow (PCF) can be found, with the exception of recent studies mainly focused on transient aspects (Pereira *et al.* 2017*a*,*b*,*c*) and elastic instability (Jovanović & Kumar 2010; Page & Zaki 2014, 2015; Biancofiore, Brandt & Zaki 2017) of drag-reduced PCFs. Evidently, PCF is one of the canonical wall-bounded flows, driven by two parallel counter-moving infinite flat plates without an imposed pressure gradient. It is also one of the most representative prototypes for studies of many different aspects of fundamental fluid mechanic problems, including hydrodynamic stability and flow transition and self-sustained mechanism of near-wall turbulence (Hamilton, Kim & Waleffe 1995; Waleffe 1997; Stone, Waleffe & Graham 2002). Despite the simplicity of the geometry, detailed study of the flow dynamics of PCF at high Reynolds number (Re) is challenging. In experiments, researchers usually use a moving belt to drive the flow; hence, the deformation of the belt moving at high speed makes it difficult to attain high Re without complications arising from fluid–wall interactions. The existence of large-scale structures (LSSs) in drag-reduced PCF requires large computational domains typically several times larger than those required for simulation of drag-reduced plane Poiseuille flow (PPF), making DNS at high Re a formidable task (Bech *et al.* 1995; Tsukahara,

https://doi.org/10.1017/jfm.2018.242 Published online by Cambridge University Press

Kawamura & Shingai 2006; Avsarkisov *et al.* 2014). These issues are undoubtedly related to the limited research on drag-reduced PCF to date as compared to other canonical wall-bounded flows, such as channel and pipe flows, especially at high *Re* (Bech *et al.* 1995; Komminaho, Lundbladh & Johansson 1996; Tsukahara *et al.* 2006; Avsarkisov *et al.* 2014; Pirozzoli, Bernardini & Orlandi 2014).

It has been suggested that the coherent structures, which are essential to sustaining the near-wall turbulence (primarily in the buffer layer), are basically the same for canonical wall-bounded turbulent flows, such as turbulent PPF and PCF (Hamilton *et al.* 1995; Waleffe 1997; Stone *et al.* 2002; Monty *et al.* 2009). In particular, it is believed that the streaks/streamwise vortices have universal characteristics in wall-bounded flows (Pizorroli, Bernardini & Orlandi 2011). Therefore, it is reasonable to speculate that similar drag-reduction-related phenomena will occur in the near-wall region of drag-reduced PCF. However, as mentioned above, much less is known about the organization of near-wall turbulence in drag-reduced PCF. On the other hand, recent findings have shown that, at sufficiently high *Re*, the outer region of canonical wall-bounded turbulent flows is characterized by LSSs with scales of the outer flow units, such as boundary-layer thickness, channel height or pipe radius (Guala, Hommema & Adrian 2006; Balakumar & Adrian 2007; Pizorroli *et al.* 2011; Wu, Baltzer & Adrian 2012; Pirozzoli *et al.* 2014; Li *et al.* 2015). Although turbulence fluctuations in the outer flow region have been analysed (Jiménez & Hoyas 2008), the underlying mechanism for the formation of LSSs has yet to be determined. Some studies show that the LSSs are self-similar and can self-sustain even when the near-wall small-scale structures are quenched artificially (Hwang & Cossu 2010; Rawat *et al.* 2015; Hellström, Marusic & Smits 2016). Moreover, it has been shown that LSSs have pronounced effects on the near-wall flow (Hwang *et al.* 2016), causing deviations from the universal wall scaling (Marusic, Mathis & Hutchins 2010). Specifically, the effects of LSSs are known to be composed of linear (imprint effects, i.e. superposition of the outer fluid motions on the near-wall fluid motion; Pizorroli *et al.* 2011; Pirozzoli *et al.* 2014) and nonlinear (amplitude modulation; Mathis, Hutchins & Marusic 2009) components.

Orlandi, Bernardini & Pirozzoli (2015) performed an extensive comparison between Newtonian PCF and PPF to highlight the similarities and differences of LSSs in these canonical flows. The LSSs are known to lead to a second peak in the pre-multiplied energy spectra for both PPF and PCF. Conversely, in PPF, a very high friction Reynolds number of order 10^3 is a prerequisite for the LSSs to be distinguishable and energetically significant. In contrast, the LSSs appearing in PCF are distinct even at a much lower Reynolds number, making PCF the ideal flow for mechanistic examination of the effects of LSSs via DNS in wall-bounded turbulent flows.

Another striking difference between PCF and PPF is the occurrence of LSSs in the ‘bulk flow’. Specifically, in PCF, large-scale streaks emerge in the channel centre, and roll cells occupy the entire gap (Komminaho *et al.* 1996; Kitoh, Nakabyashi & Nishimura 2005; Tsukahara *et al.* 2006; Kitoh & Umeki 2008). Neither of these two LSSs has been found in PPF (Avsarkisov *et al.* 2014; Niebling *et al.* 2014; Pirozzoli *et al.* 2014; Kawata & Alfredsson 2016). Furthermore, such LSSs have an intriguing influence on the turbulent dynamics, especially in the outer region where roll cells lead to marked differences in heat transfer (Liu 2003; Debusschere & Rutland 2004; Pasinato 2011) and particle dispersion (Bernardini, Pirozzoli & Orlandi 2013; Hosseiniebalam, Hassanzadeh & Ghaffarpasand 2014).

Motivated by the aforementioned facts, DNS of drag-reduced PCF has been performed to investigate the drag-reduction-related features in the near-wall and

https://doi.org/10.1017/jfm.2018.242 Published online by Cambridge University Press

core regions and to make a detailed comparison with drag-reduced PPF. Furthermore, in the present work, we have focused on the effects of LSSs on near-wall turbulence, which has been a highly debated issue in the past decade for Newtonian turbulence (Marusic *et al.* 2010; Pirozzoli *et al.* 2014; Rawat *et al.* 2015; Smits 2015) and to date remains unclear for polymer-induced, drag-reduced flows.

2. Problem formulation and computational details

In accordance with our prior studies of polymer-induced turbulent drag reduction (Li, Sureshkumar & Khomami 2006; Liu & Khomami 2013*a*,*b*; Li *et al.* 2015), the FENE-P (finitely extensible nonlinear elastic-Peterlin) constitutive equation is used to model the polymer contribution to total stress. We have chosen h, h/U_w, U_w and ρU_w^2 as scales for length, time, velocity $\boldsymbol{u}$ and pressure p, respectively. Here h denotes the half-height of the channel, U_w represents the wall translation velocity and ρ denotes the solution density. Further, we scale the conformation tensor $\boldsymbol{C}$, which represents the ensemble average of the second moment of the end-to-end vector of the polymer chains, with respect to kT/H, where k, T and H denote the Boltzmann constant, absolute temperature and Hookean spring constant of the elastic dumbbell model, respectively. The resulting dimensionless equations governing the motion of an incompressible FENE-P fluid are as follows:

$$\frac{\partial \boldsymbol{u}}{\partial t} + \boldsymbol{u}\cdot\nabla\boldsymbol{u} = -\nabla P + \frac{1}{Re}\nabla^2\boldsymbol{u} + \nabla\cdot\boldsymbol{\tau}^p \tag{2.1}$$

and

$$\frac{\partial \boldsymbol{C}}{\partial t} = -\boldsymbol{u}\cdot\nabla\boldsymbol{C} + \boldsymbol{C}\cdot\nabla\boldsymbol{u} + (\nabla\boldsymbol{u})^{\mathrm{T}}\cdot\boldsymbol{C} - \boldsymbol{\tau}^p. \tag{2.2}$$

The polymer stress tensor $\boldsymbol{\tau}^p$ is obtained as

$$\boldsymbol{\tau}^p = \frac{1-\beta}{\beta}\frac{1}{ReWe}\left(\frac{L^2-3}{L^2-\mathrm{trace}(\boldsymbol{C})}\boldsymbol{C} - \boldsymbol{I}\right), \tag{2.3}$$

where $\beta = \eta_s/\eta_t$, with η_s and η_p being respectively the solvent and polymeric contributions to the total viscosity η_t, L is the maximum chain extensibility; the Weissenberg number is defined as $We = \lambda U_w/h$ (the ratio of the elastic relaxation time λ relative to the flow time scale h/U_w) and the Reynolds number as $Re = \rho U_w h/\eta_s$. A fully spectral, three-dimensional parallel algorithm (Li *et al.* 2006, 2015; Liu & Khomami 2013*a*,*b*; Teng *et al.* 2015) is employed to solve the governing equations, i.e. Chebyshev polynomials in the wall-normal (y-) direction and Fourier series in the streamwise (x-) and spanwise (z-) directions. These equations are also supplemented by the no-slip boundary conditions at the walls, as well as periodic boundary conditions in the x- and z- directions. The initial condition is a fully developed turbulent Newtonian PCF with introduction of a unit conformation tensor (Nguyen *et al.* 2016; Pereira *et al.* 2017*a*,*b*).

In addition, a diffusive term $\kappa\nabla^2\boldsymbol{C}$ is added to equation (2.2) in the bulk flow region to numerically stabilize the integration of the conformation tensor evolution equation. In order to retain the essential dynamics resulting from flow–microstructure coupling while maintaining numerical stability, the value of the scalar stress diffusivity κ should be chosen to be as low as possible (Li *et al.* 2006). In the present study, a

https://doi.org/10.1017/jfm.2018.242 Published online by Cambridge University Press

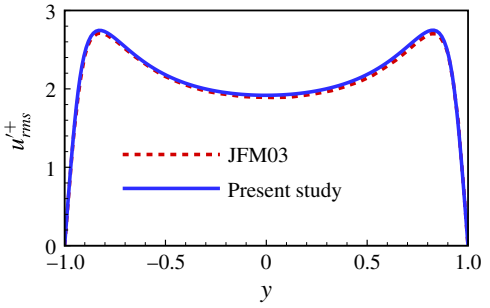


FIGURE 1. (Colour online) Comparison of root-mean-square (r.m.s.) value of streamwise velocity fluctuation with that obtained by Hu, Morfey & Sandham (2003). The superscript '+' is hereafter used to denote the quantity non-dimensionalized by the viscous length scale $\delta = \nu_s/u_\tau$; the friction velocity is defined as $u_\tau = \sqrt{\tau_w/\rho}$ where τ_w is the total wall stress; the overbar denotes ensemble averaging.

κ value corresponding to a Schmidt number of $Sc = 1/(\kappa Re) = 0.15$ is used for all the calculations. This Schmidt number is of the same order as the values used by Li *et al.* (2006) and Thais *et al.* (2012). Note that the original constitutive equation without the diffusive term is applied at the walls, thus no boundary conditions are imposed at the walls for $\boldsymbol{C}$.

In the present study, the Reynolds number is fixed at 1300 (Komminaho *et al.* 1996; Tsukahara *et al.* 2006), and the Weissenberg number is varied from 0 to 7, corresponding to a low elasticity number, i.e. $E = We/Re = 0$–0.005. We use a large value of $L = 120$ and $\beta = 0.9$ in that the polymeric solution has a nearly shear-independent viscosity (Li *et al.* 2006, 2015; Liu & Khomami 2013*a*,*b*). To capture the LSSs in the core region, a much larger computational domain is necessary for PCF as compared to PPF (Komminaho *et al.* 1996; Tsukahara *et al.* 2006; Avsarkisov *et al.* 2014). Based on extensive test calculations, the computational domain is set as $L_x \times L_y \times L_z = 40\pi \times 2 \times 6\pi$ for the streamwise, wall-normal and spanwise directions, respectively. This corresponds to a grid size of $1024 \times 129 \times 256$. A time step of $\Delta t = 0.01$ is used for the present calculations. Basically, our simulations have a mesh size 8 times larger than that of the drag-reduced PPF simulations conducted by Li *et al.* (2006, 2015). This results in a significant increase in computational cost; hence, limiting the maximum Re that DNS of drag-reduced PCF can access with today's most powerful supercomputers.

The code used in the present study has been extensively validated and successfully used in previous simulations of drag-reduced PPF (Li *et al.* 2006, 2015). In the present work, code validation includes calculation of Newtonian PCF under the same conditions as the comprehensive study by Hu *et al.* (2003). All of our simulation results are in full agreement with the aforementioned study. Specifically, both the streamwise velocity fluctuations (see figure 1) and the scales of the coherent structures (see figure 2), namely, the streamwise and spanwise scales determined by two-point correlations $R_{uu}(\Delta x)$ and $R_{uu}(\Delta z)$, show similar behaviour. The two-point correlations are defined as

$$R_{uu}(\Delta x) = \frac{\overline{u'(x, z)u'(x + \Delta x, z)}}{\overline{u'^2}} \tag{2.4}$$

https://doi.org/10.1017/jfm.2018.242 Published online by Cambridge University Press

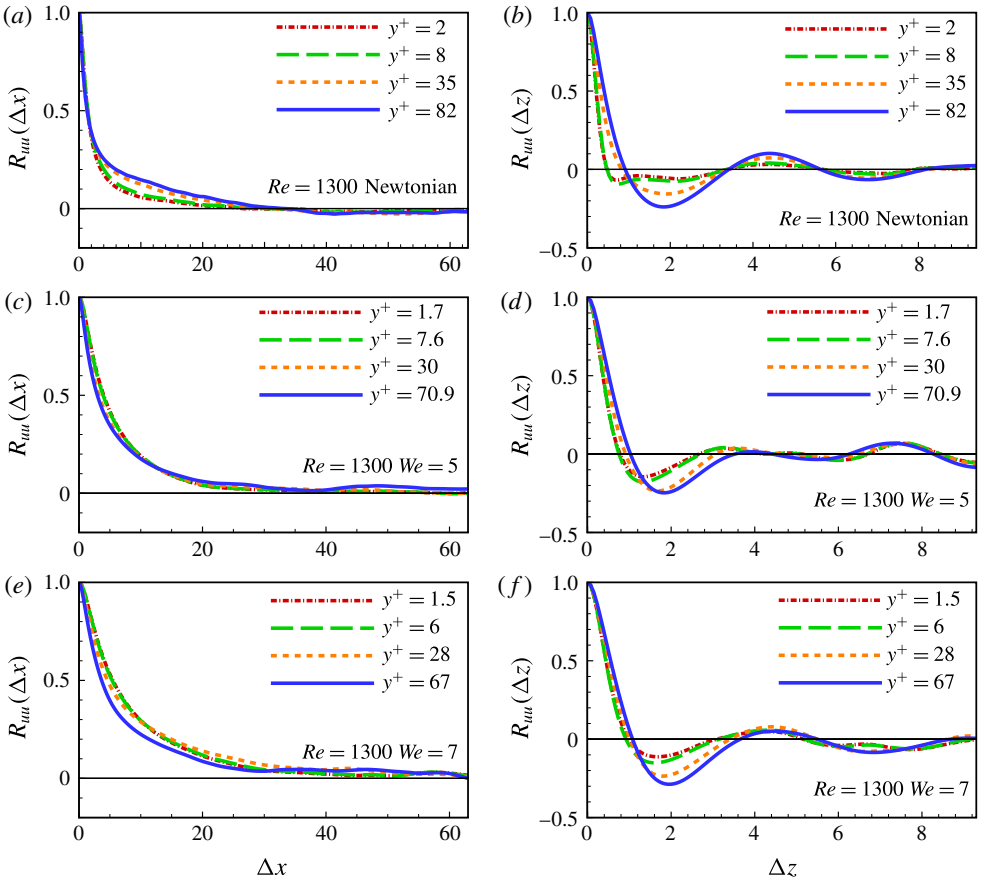


FIGURE 2. (Colour online) The two-point correlations of the streamwise velocity fluctuation for Newtonian PCF (*a*,*b*), and drag-reduced PCFs of $We = 5$ (*c*,*d*) and $We = 7$ (*e*,*f*).

and

$$R_{uu}(\Delta z) = \frac{\overline{u'(x, z)u'(x, z + \Delta z)}}{\overline{u'^2}}. \tag{2.5}$$

Hereafter, the superscript ‘′’ denotes the fluctuating part. As indicated in figure 2(*a*), the zero value of $R_{uu}(\Delta x)$ occurs at approximately 35 in the channel centre for Newtonian PCF, pointing to a streamwise scale of 70 for the large-scale coherent structures. This prediction is consistent with a value of $40 \sim 65$ reported in prior studies (Tsukahara *et al.* 2006; Avsarkisov *et al.* 2014). The first minimum of $R_{uu}(\Delta z)$ for Newtonian PCF appears at approximately 0.73 (see figure 2*b*) in the buffer layer ($y^+ = 8$). This corresponds to the spanwise scale of approximately 120 in wall units for near-wall coherent structures. This estimate is basically consistent with the well-accepted value of $\sim$100 in wall-bounded shear flows (Kline *et al.* 1967; Kim, Moin & Moser 1987; Tiederman 1990; Jiménez & Moin 1991; Hamilton *et al.* 1995; Tsukahara *et al.* 2006; Monty *et al.* 2009). Note that PCF of low *Re*, exhibits near-wall structures evidently influenced by the LSSs (Komminaho *et al.* 1996).

https://doi.org/10.1017/jfm.2018.242 Published online by Cambridge University Press

We	$\Delta x^+ \times \Delta y^+_{max} \times \Delta z^+$	Re_τ	$DR\,\%$
Newtonian	$10.1 \times 2 \times 6.1$	82.3	—
2	$10 \times 2 \times 6.1$	81.6	1.7
5	$8.7 \times 1.6 \times 5.3$	70.9	26
7	$8.2 \times 1.7 \times 5$	67.0	34

TABLE 1. Numerical parameters, where the friction Reynolds number is defined as $Re_\tau = \rho u_\tau h/\eta_s$.

In consequence, the spanwise scale of near-wall coherent structures of 100 wall units is masked by the imprint effects of LSSs (Pizorroli *et al.* 2011); this phenomenon is discussed in detail in § 5.

Figure 2 also clearly demonstrates that in all of our calculations $R_{uu}(\Delta x)$ and $R_{uu}(\Delta z)$ decay to approximately zero at half of the domain size in the streamwise and spanwise directions. Hence, the computational domain used is sufficiently large to contain the LSSs appearing in the core region. In fact, to capture the scale enhancement due to drag reduction, the computational domain has been set larger than the previous DNS of Newtonian PCF (Avsarkisov *et al.* 2014). The precise values of key parameters in our simulations are provided in table 1.

3. Drag-reduction-related features in PCF

Similar to PPF, addition of flexible polymers can lead to drag reduction in PCF. As expected, the polymer-induced drag reduction is enhanced with the increase of We (see table 1). The extent of drag reduction rate is computed as follows:

$$DR\,\% = \frac{\tau_{w0} - \tau_w}{\tau_{w0}} = \frac{Re_{\tau 0}^2 - Re_\tau^2}{Re_{\tau 0}^2}, \tag{3.1}$$

where $\tau_w = \rho \nu_s (\mathrm{d}\overline{u}/\mathrm{d}y) + \overline{\tau_{xy}^p}$ is the total wall stress, with $\overline{\tau_{xy}^p}$ being the polymeric stress contribution. τ_{w0} and $Re_{\tau 0}$ correspond respectively to the wall stress and the frictional Reynolds number of Newtonian PCF. It is found that $DR\,\%$ increases from 1.7 % to 26 %, then to 34 % when We varies from 2 to 5, and then to 7 (see table 1). Hence, the drag reduction observed in PCF should be categorized as low drag reduction (LDR), namely, $DR\,\% < 40\,\%$ (Dubief *et al.* 2004; White & Mungal 2008; Dallas *et al.* 2010; Pereira *et al.* 2017*b*).

A close examination of the overall force (or stress) is required to investigate the turbulence dynamics of drag-reduced flows. The force balance for drag-reduced PCF can be expressed as:

$$\frac{\mathrm{d}\overline{u}^+}{\mathrm{d}y^+} - \overline{u'v'}^+ + \overline{\tau_{xy}^p}^+ = 1, \tag{3.2}$$

where $\overline{u}^+$ is the mean flow velocity in wall units. The left-hand-side terms of equation (3.2) are in sequence: the shear stress $S_m = \mathrm{d}\overline{u}^+/\mathrm{d}y^+$ coming from mean flow shear, the Reynolds stress $S_t = -\overline{u'v'}^+$ accounting for turbulent momentum transfer and the polymer stress $S_p = \overline{\tau_{xy}^p}^+$, which vanishes for Newtonian PCF.

Clearly, an overall force balance is achieved in all the calculations; the total stress (i.e. the sum of the shear stress S_m, the Reynolds stress S_t and the polymer stress S_p)

https://doi.org/10.1017/jfm.2018.242 Published online by Cambridge University Press

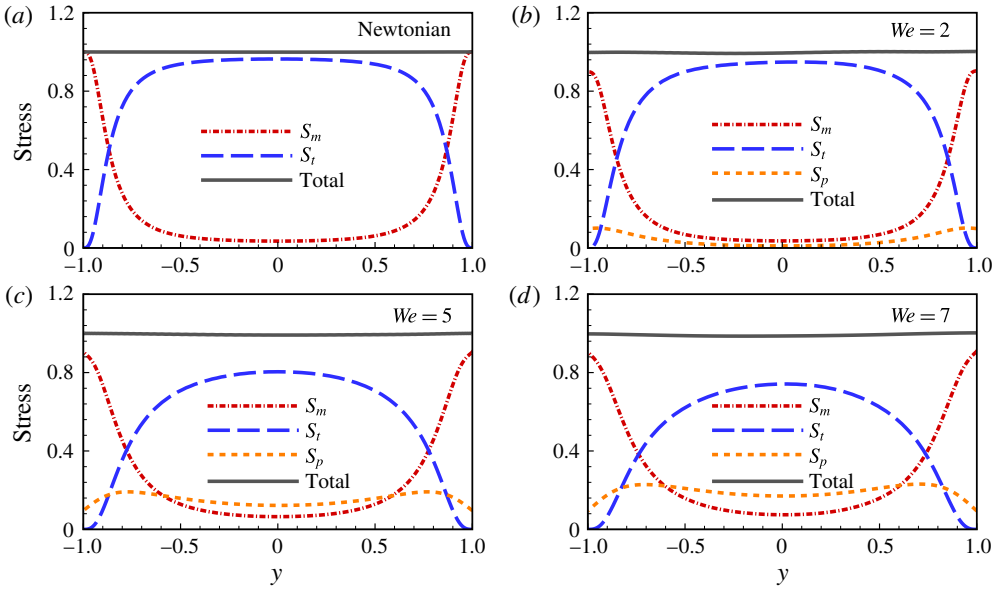


FIGURE 3. (Colour online) Overall force balance for Newtonian PCF (*a*), and drag-reduced PCFs with $We = 2$ (*b*), $We = 5$ (*c*) and $We = 7$ (*d*).

is equal to unity over the entire channel (see figure 3). This clearly demonstrates that fully stationary states have been realized. Similar to PPF (Li *et al.* 2006, 2015), the Reynolds stress has a dominant contribution in the core region for the Newtonian case – approximately 90 % of the total stress. As We is increased, S_t decreases continuously and reaches a value of less than 80 % of the total stress. This indicates that polymer additives reduce turbulent momentum transfer. On the other hand, a substantial enhancement of polymer stress is observed when We increases from 0 to 7. Specifically, for $We = 7$, S_p contributes approximately 20 % to the total stress in the core region. Moreover, a non-zero S_m value occurs at the channel centre and becomes greater, indicating a growth of mean flow shear with the increase of We. Thus, the polymer stress and the mean flow shear are expected to have major effects on the bulk flow of drag-reduced PCF.

The flow response to the addition of polymer is examined (see figure 4) by observing the changes in the mean flow velocity $\overline{u}$. Specifically, the gradient of mean flow velocity decreases at the wall with a commensurate decrease in wall shear stress (see figure 4*a*). In contrast, in the core region the $\overline{u}$ gradient increases, pointing to an enhanced S_m, as shown in figure 3. Figure 4(*b*) presents the log plot of $\overline{u}^+$ for different We. It has been demonstrated that the mean flow velocity collapses into the classical log law in the outer region for Newtonian PCF (Avsarkisov *et al.* 2014). As We is increased from 0 to 7, $\overline{u}^+$ increases in the outer region, resulting in a deviation from the log law while trending towards the well-known Virk law (Virk 1975; Ptasinski *et al.* 2003). Note that, for the LDR regime of PPF, the log-law profile of $\overline{u}^+$ in outer region has a slope the same as that of the Newtonian case; however, this is not so for drag-reduced PCF.

To examine the turbulent motion in drag-reduced PCF, the r.m.s. values of velocity fluctuations are shown in figure 5. For PPF of LDR, the polymeric additive is found to suppress the energy redistribution from the streamwise to the wall-normal and

https://doi.org/10.1017/jfm.2018.242 Published online by Cambridge University Press

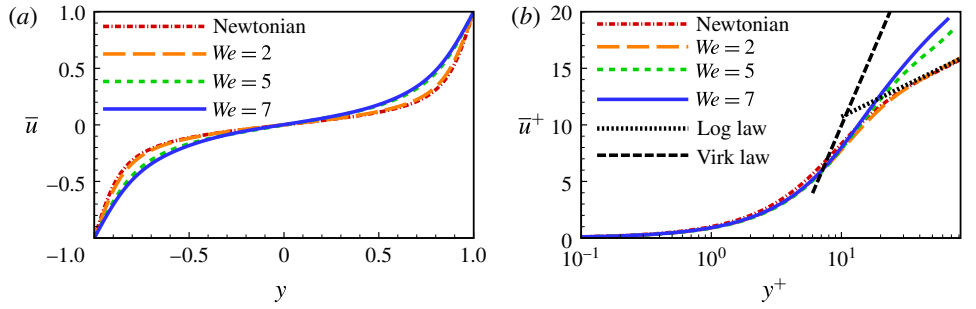


FIGURE 4. (Colour online) Mean streamwise velocity $\overline{u}$ profile across the channel (*a*) and its log plot in the lower half of the channel versus the wall-normal distance (*b*), here $\overline{u}^+ \equiv (\overline{u} + U_w)^+$. The log law corresponds to $\overline{u}^+ = (1/k)\ln(y^+) + C$ with $k = 0.41$ and $C = 5.1$ (Avsarkisov *et al.* 2014) and Virk law corresponds to $\overline{u}^+ = 11.7\ln(y^+) - 17$ (Virk 1975).

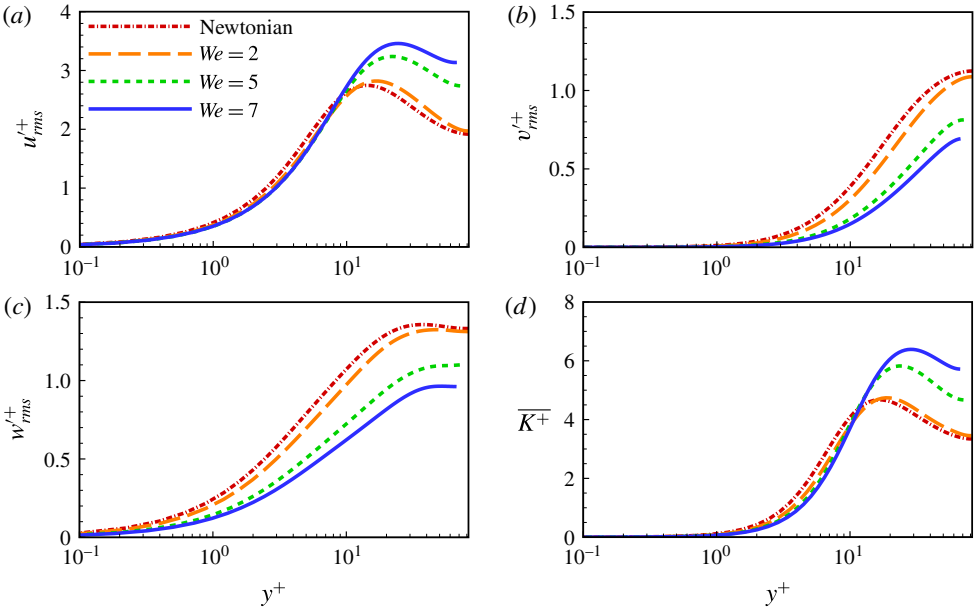


FIGURE 5. (Colour online) Profiles of r.m.s. values of streamwise (*a*), wall-normal (*b*) and spanwise (*c*) velocity fluctuations, and turbulent kinetic energy (*d*).

spanwise fluctuating motions, which leads to an increase in streamwise velocity fluctuation in the buffer and log layers and a decrease in the other two components (Min *et al.* 2003*b*; Stone *et al.* 2004; Li *et al.* 2006, 2015). In the high drag reduction (HDR) regime of PPF, all three components of r.m.s. velocities are suppressed. For drag-reduced PCF, the r.m.s. value of velocity fluctuations exhibits polymer-induced variations in a manner similar to that of PPF at LDR. Namely, introducing polymer additives serves to enhance the r.m.s. value of streamwise velocity fluctuations, i.e. the streamwise fluctuating motions, and to suppress the other two components (see figure 5*a–c*). With the increase of *We*, this effect of polymer additives becomes more pronounced. Moreover, the peak values of the turbulent kinetic energy (see figure 5*d*)

https://doi.org/10.1017/jfm.2018.242 Published online by Cambridge University Press

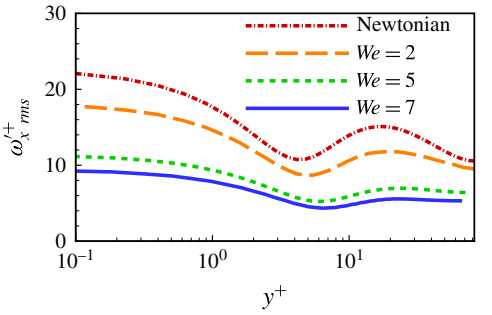


FIGURE 6. (Colour online) Distribution of r.m.s. value of streamwise vorticity fluctuation.

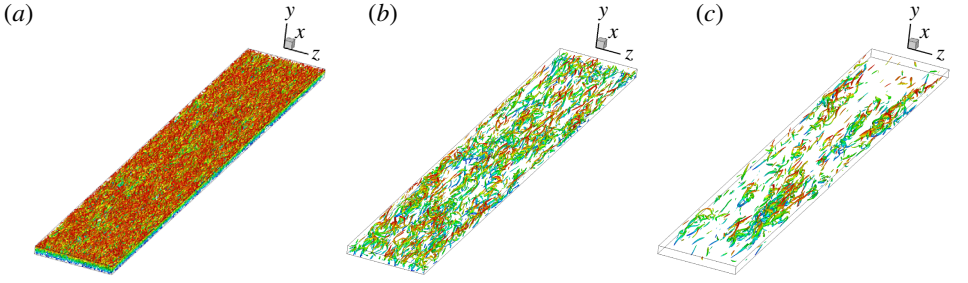


FIGURE 7. (Colour online) Vortical (elliptical) structures visualized by instantaneous Q-criterion with $Q = 0.1$ and coloured by the distance to the lower wall for Newtonian PCF (*a*), $We = 5$ (*b*) and $We = 7$ (*c*).

shift away from the wall, indicating the broadening of the buffer layer. This near-wall turbulence behaviour has also been found in drag-reduced PPF.

The effect of polymer elasticity on near-wall quasi-streamwise vortices (QSVs) can be examined by the r.m.s. value of streamwise vorticity fluctuation ($\omega_{x\ rms}^{\prime+}$) (see figure 6). According to Kim *et al.* (1987), the y- positions of the local minimum and maximum of $\omega_{x\ rms}^{\prime+}$ correspond to the ensemble-averaged locations of the edge and centre of the QSVs, respectively, and their distance is roughly proportional to the size of the QSVs. When We is increased from 0 to 7, $\omega_{x\ rms}^{\prime+}$ decreases substantially, and the difference between the local minimum and maximum of $\omega_{x\ rms}^{\prime+}$ becomes more and more subtle. This points to a drag-reduction-related weakening process of QSVs. The weakening of QSVs is a common feature in drag-reduced shear flow (Stone *et al.* 2004), that results in less energetic ejection and sweep events in the buffer layer. Moreover, the local minimum and maximum of $\omega_{x\ rms}^{\prime+}$ shift away from the wall, as a result of the broadening of the buffer layer. Note that PCF and PPF share the same polymer-induced behaviours of $\omega_{x\ rms}^{\prime+}$ (Min *et al.* 2003*b*; Li *et al.* 2006, 2015; Dallas *et al.* 2010). This similarity supports studies in that the near-wall coherent structures are essentially the same for the self-sustaining mechanism of wall-bounded turbulence (Hamilton *et al.* 1995; Stone *et al.* 2002). The weakening of near-wall QSVs with the increase of We can also been visualized by the instantaneous Q-plot for vortical (elliptical) structures of $Q = 0.1$ (see figure 7). Together with the similar weakening of extensional (hyperbolic) structures (not visualized here), this feature confirms that enhanced drag reduction is commensurate with a phenomena of

https://doi.org/10.1017/jfm.2018.242 Published online by Cambridge University Press

flow parabolization, as found by Pereira *et al.* (2017*b*,*c*) in their study of transient evolution of viscoelastic PCF.

In the core region, however, the behaviour of $\omega_{x\,rms}^{\prime+}$ is markedly different between drag-reduced PPF and PCF. As for viscoelastic PPF at LDR, $\omega_{x\,rms}^{\prime+}$ in the core region is much less than that in the near-wall region (Li *et al.* 2006, 2015; Dallas *et al.* 2010). However, for the drag-reduced PCFs considered here, the values of $\omega_{x\,rms}^{\prime+}$ in the core region and near-wall region are comparable (see figure 6). This difference is associated with the presence of roll cells that appear in the core region of PCF. Such roll cells behave like counter-rotating QSVs of a much larger scale and contribute to generate additional streamwise vorticity fluctuations in the core region. The strength of QSVs in the core region decreases with increasing *We* (see figure 6); this is consistent with the trend observed in the simplified linear problem of roll–streak interaction in viscoelastic Couette flow (Page & Zaki 2014).

The scale of coherent structures changing with the increasing polymer elasticity can be quantified by the two-point correlations. Specifically, an increase of spanwise scale occurs for the near-wall coherent structures. In figure 2(*b*), the first minimum of near-wall $R_{uu}(\Delta z)$ is indicative of the spanwise spacing of near-wall coherent structures. As stated above, the first minimum of $R_{uu}(\Delta z)$ for $y^+ = 8$ occurring at $\Delta z \approx 0.73$ indicates a spanwise spacing of $\Delta z^+ \approx 120$ for the near-wall coherent structures. At the channel centre ($y^+ = 82$), $R_{uu}(\Delta z)$ has its first minimum occurring at $\Delta z \approx 1.85$, corresponding to a spanwise scale of LSSs in the core region of $\Delta z \approx 3.70$ for LSSs. As *We* is increased from 0 to 7, the near-wall coherent structures scale grows in the spanwise direction as the first minimum of $R_{uu}(\Delta z)$ occurs at a larger value of Δz; however, spanwise scales of the core-region LSSs remain almost unaltered. Increase in spanwise scale of near-wall coherent structures is a common feature of drag-reduced PPF (Li *et al.* 2006; White & Mungal 2008). The results shown here confirm that the same is true for drag-reduced PCF.

4. Flow behaviour in the core region

As addressed above, differences between turbulent PCF and PPF exist mainly in the core region. Large-scale streaks and roll cells have been found in the core region of PCF but not in PPF. This is the main difference between PCF and PPF. Another significant difference is that a non-zero mean flow shear rate is present in PCF. To this end, in the discussion that follows, turbulence dynamics in the core region of drag-reduced PCF is scrutinized.

The large-scale streaks can be visualized at the channel centre by the streaky patterns of positive and negative streamwise velocity fluctuations alternating along the spanwise direction (see figure 8). As *We* is increased from 0 to 7, the longitudinal length scales of the large-scale streaks increase, making the streaks more distinguishable. This change indicates an enhanced growth of large-scale streaks due to polymer elasticity, consistent with the findings of a recent study on instability of streak evolution (Page & Zaki 2014). In parallel, the intensity of the streaks indicates an enhancement of streamwise fluctuating motions.

To better understand PCF polymer dynamics, mean values of the conformation tensor components and their fluctuations are examined (see figure 9). Specifically, it can be seen in figure 9(*a*) that the mean value of C_{xx} has its maximum in the wall region at low *We*, namely, $We = 2$, and in the buffer layer at high *We* ($We = 7$). This feature is basically the same as drag-reduced PPF (Dallas *et al.* 2010). Note for drag-reduced PCF, the mean value of C_{xx} in the core region is approximately half of

https://doi.org/10.1017/jfm.2018.242 Published online by Cambridge University Press

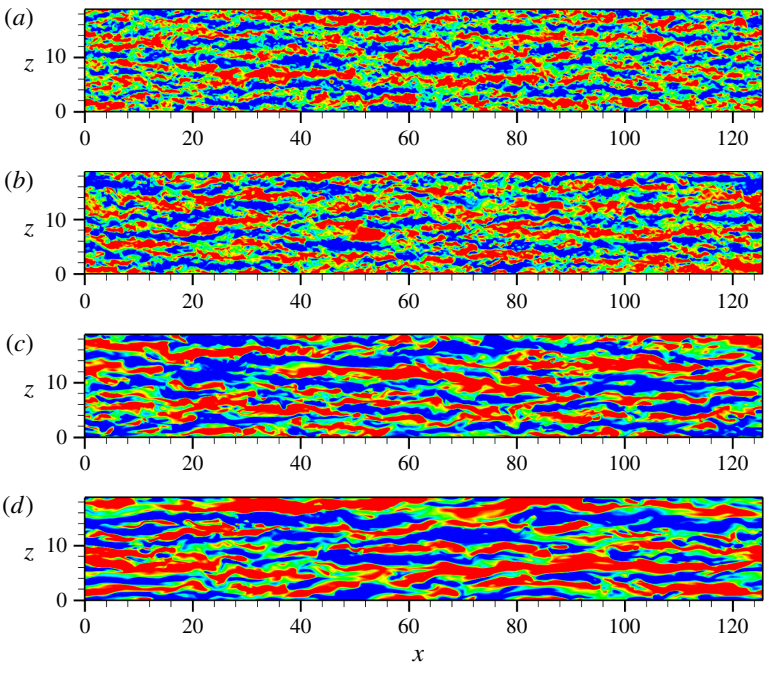


FIGURE 8. (Colour online) Visualization of streaky structures by instantaneous streamwise velocity fluctuation in the x–z plane at channel centre, (a) Newtonian flow, (b) $We = 2$, (c) $We = 5$ and (d) $We = 7$. Twenty contours are shown in $(-0.1, 0.1)$.

that of the near-wall region, while the mean values of C_{yy} and C_{zz} (see figures 9*c* and 9*e*) are approximately zero in the wall region with their maxima occurring at the channel centre. This is strikingly different from the case of drag-reduced PPF (Li *et al.* 2006; Dallas *et al.* 2010). The large mean values of C_{xx}, C_{yy} and C_{zz} occurring at the channel centre are ascribed to high polymer stretching related to the mean flow shear and LSSs in the core region. Basically, the fluctuations of C_{xx}, C_{yy} and C_{zz} have similar distributions to the main values of these components in the conformation tensor. Thus, mean polymer stretch and its fluctuating part are enhanced in turbulent PCF with the increase of *We*.

To examine the influence of polymer stretch on energy exchange in the core region, the budgets of mean kinetic energy (MKE), turbulent kinetic energy (TKE) and elastic potential energy (EPE) are analysed. This has been shown to be a good starting point to advance mechanistic understanding of drag reduction in drag-reduced PPF (Dimitropoulos *et al.* 2001; Min *et al.* 2003*a*,*b*; Dallas *et al.* 2010; Tsukahara *et al.* 2011; Thais *et al.* 2012, 2013). In the following, we focus on the budget terms of key importance to the energy exchange process. Specifically, the production terms P_m^+, P_{pm}^+ and P_{pt}^+ represent energy exchange from MKE to TKE, from MKE to EPE and from TKE to EPE, respectively; ε_m^+ and D_{mv}^+ denote respectively viscous dissipation and diffusion of MKE; D_{mP}^+ and D_{mt}^+ are the mean pressure and turbulent transport terms, respectively; and D_{pm}^+ and D_{pt}^+ are the polymeric transport terms for MKE and TKE, respectively. A detailed description of the budget equations for MKE, TKE and EPE is given in appendix A.

In figure 10(*a*–*d*), the budget terms of MKE and TKE for Newtonian flow are compared with those of drag-reduced PCF at $We = 7$; the budget terms of EPE are also

https://doi.org/10.1017/jfm.2018.242 Published online by Cambridge University Press

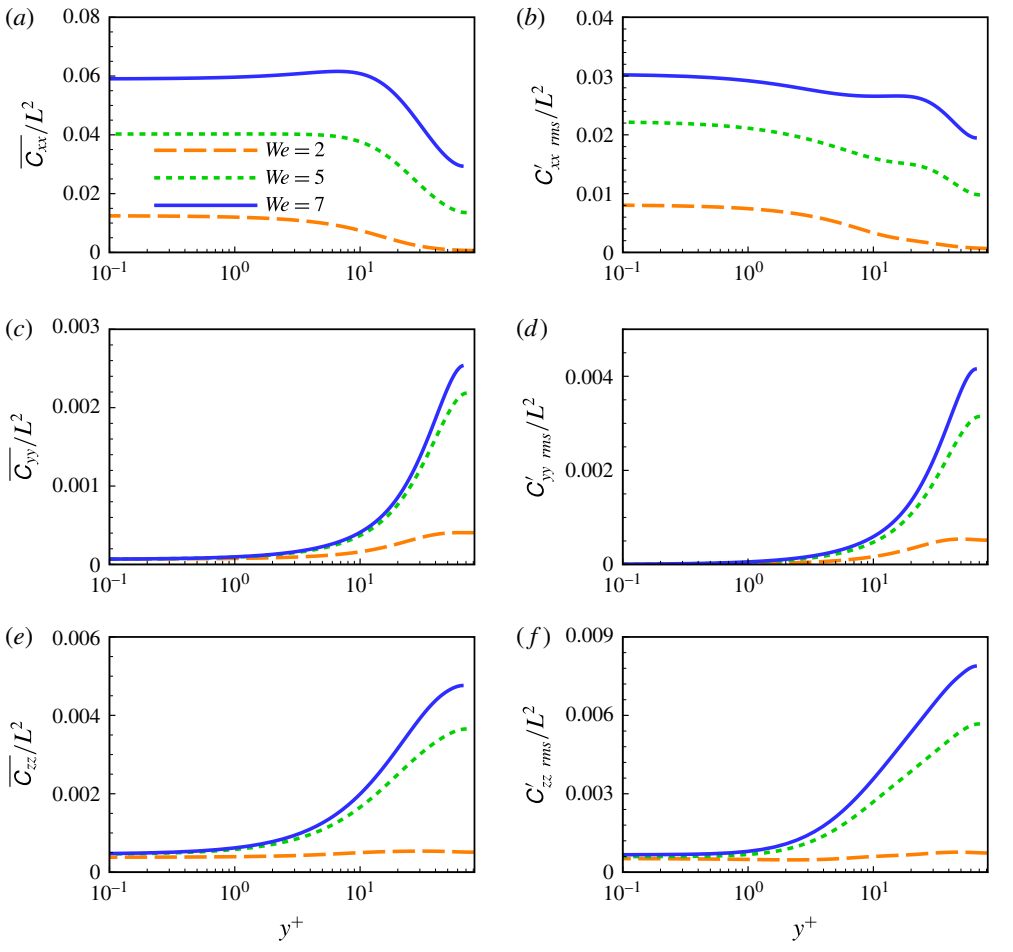


FIGURE 9. (Colour online) Mean and r.m.s. values of the conformation tensor component C_{xx}, C_{yy} and C_{zz} for different We.

plotted in figure 10(*e*). The balances achieved in these three budgets provide a further evidence that statistically steady states have been realized in our calculations. Here, some differences between PCF and PPF can be clearly seen. For the budget of MKE, it is shown (see figure 10*a*) that viscous diffusion D^+_{mv} is positive (i.e. a source term) across the channel for Newtonian PCF; however, for PPF, this term changes from positive to negative as one moves away from the wall (Thais *et al.* 2013). In contrast, turbulent transport term D^+_{mt} is positive across the channel for PPF but changes from positive to negative for PCF. Moreover, non-zero values of P^+_m and ε^+_m can be observed in the core region of PCF; however, for PPF, all the budget terms of MKE approach zero in this region. This is the most distinct difference between PCF and PPF, and it originates from the non-zero mean flow shear in the core region, as discussed above.

With respect to the MKE budget of drag-reduced PCF (see figure 10*b*), two extra terms are added, namely, the polymer transport term D^+_{pm} and energy production term P^+_{pm}. $-P^+_{pm}$ is negative across the channel, which means that the polymer chains absorb energy from the MKE in the entire domain. In the core region, $-P^+_{pm}$ is comparable to

https://doi.org/10.1017/jfm.2018.242 Published online by Cambridge University Press

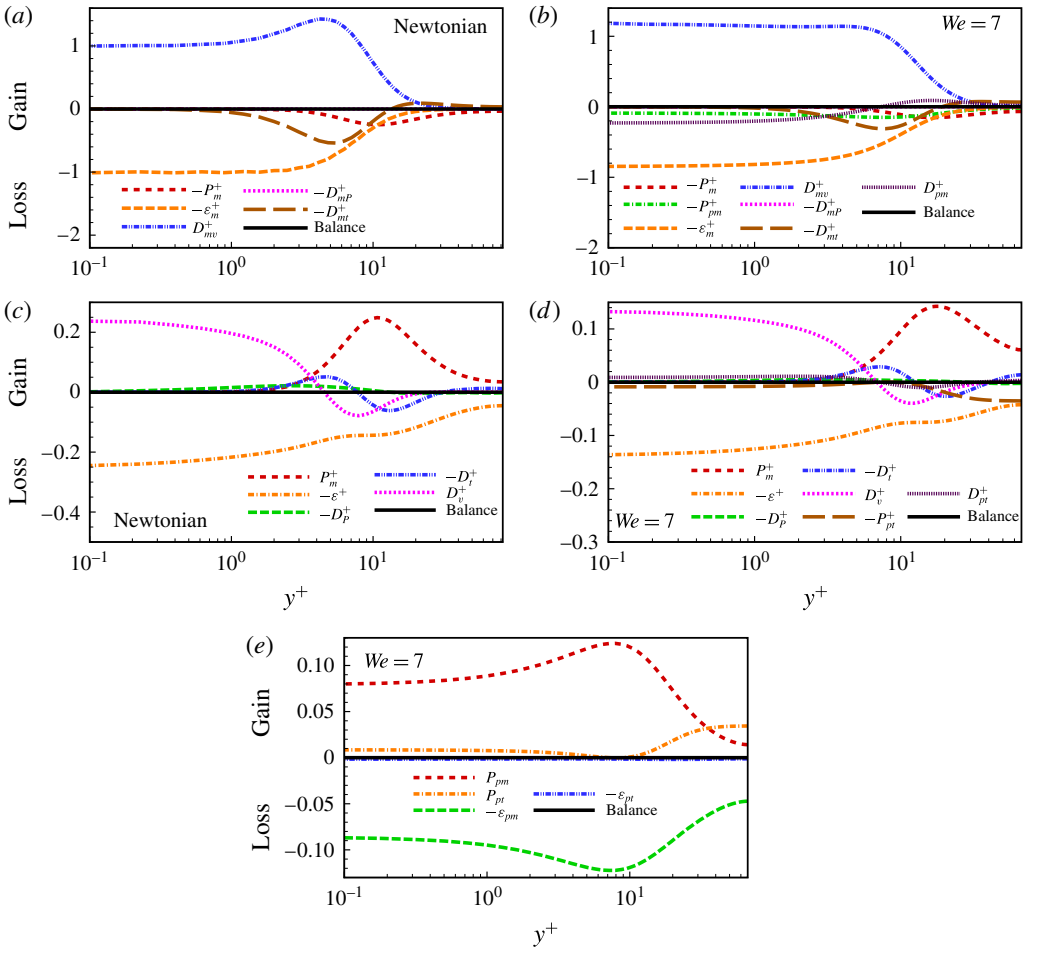


FIGURE 10. (Colour online) The budgets for mean kinetic energy K_m^+ (*a*,*b*), turbulent kinetic energy K^+ (*c*,*d*) and elastic potential energy E_p^+ (*e*).

other budget terms. In contrast, drag-reduced PPF has a negligibly small value of P_{pm}^+ in the core region (Thais *et al.* 2013). This comparison also highlights the difference of flows in the core region between viscoelastic PCF and PPF. Note in figure 10(*b*) that the polymer transport term D_{pm}^+ changes its sign from negative to positive when one moves away from the wall; the opposite is true in the case of PPF.

For Newtonian PCF, the budget of TKE of is very similar to that of PPF (Thais *et al.* 2013), except in the core region where TKE has production and dissipation terms that are very large for PCF although negligibly small for PPF (see figure 10*c*). For viscoelastic PCF, two polymer-related terms, the energy exchange term, P_{pt}^+ and the polymeric transport term, D_{pt}^+, are added. The P_{pt}^+ term has been regarded to quantify energy exchange between TKE and EPE. Specifically, negative $-P_{pt}^+$ means that the kinetic energy carried by fluctuating motions is absorbed and stored as elastic potential energy of stretched polymer chains; positive $-P_{pt}^+$ means that elastic potential energy is released from the stretched polymer chains to turbulent motions. Thus, the P_{pt}^+ term is of great importance in evaluating the interaction between

https://doi.org/10.1017/jfm.2018.242 Published online by Cambridge University Press

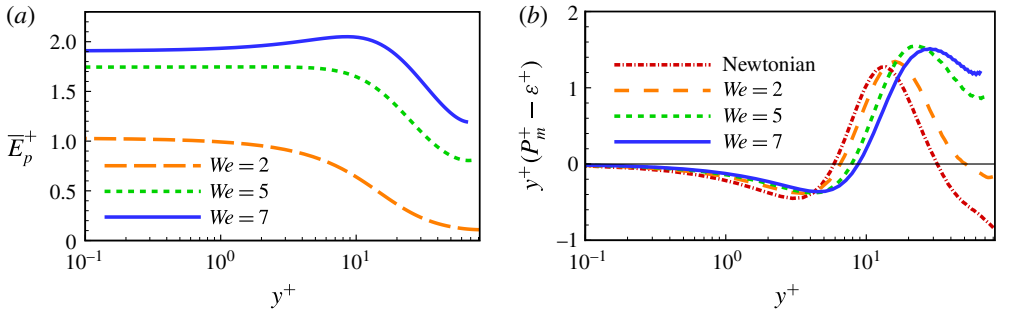


FIGURE 11. (Colour online) The mean elastic potential energy (*a*) and pre-multiplied energy production excess (*b*).

turbulent motions and polymer stretching (Min *et al.* 2003*a*,*b*; Dallas *et al.* 2010; Tsukahara *et al.* 2011). According to Tsukahara *et al.* (2011), the flow domain of drag-reduced PPF can be divided along the vertical direction into three regions based on the sign of P_{pt}^+, namely, the wall vicinity region with $-P_{pt}^+ < 0$, the near-wall region with $-P_{pt}^+ > 0$ and the core region with $-P_{pt}^+ < 0$. Therefore, the polymer chains absorb energy from turbulence fluctuations in the near-wall region, and begin to release their stored energy back to turbulence when they migrate away from the wall before approaching the core region.

For drag-reduced PCF, three similar regions are also seen in figure 10(*d*), although the second region is not clearly distinguishable due to its very narrow interval and small magnitude. However, in the core region $-P_{pt}^+$ has a negative increase toward the channel centre, while for PPF it decreases in magnitude to zero. In figure 10(*d*), the minimum of $-P_{pt}^+$ occurring at the channel centre indicates that the polymer chains have the largest rate of energy absorption from turbulence in the core region. This intriguing phenomenon accounts for the considerable polymer stretch in the core region of PCF, as indicated in figure 9. At the same time, the production term P_m^+ becomes larger in the core region to maintain the budget balance, which in turn leads to a larger production/dissipation ratio. According to Lam & Banerjee (1992), the production/dissipation ratio is indicative of the formation of streaks: the larger the ratio, the more intensive the streaks. Therefore, in the core region of PCF, production/dissipation ratio is enhanced as a consequence of significant energy absorbed from turbulence fluctuations. This provides a plausible explanation as to why the large-scale longitude streaks strengthen, as depicted in figure 8.

Figure 10(*e*) illustrates the EPE budget of $We = 7$. It is seen by P_{pm}^+ and P_{pt}^+ that the polymers practically absorb energy from the MKE and TKE in the entire channel; this energy is then dissipated by the relaxation of polymer chains from an extended to an equilibrium state. Unlike drag-reduced PPF where the largest polymer dissipation occurs at the wall (Ptasinski *et al.* 2003), the largest polymer dissipation in PCF occurs in the buffer layer. More distinct differences occur in the core region. Specifically, for drag-reduced PPF (Thais *et al.* 2013), all the EPE budget terms are trivially small in the core region; however, for drag-reduced PCF, they are large. This indicates substantial energy absorption by polymers from the MKE and TKE, which is balanced by dissipation via polymer relaxation. This polymeric behaviour can be confirmed by the distribution of the mean elastic potential energy (MEPE; see figure 11*a*), where the MEPE has a value in the core region of two thirds of its wall

https://doi.org/10.1017/jfm.2018.242 Published online by Cambridge University Press

value. In contrast, for PPF, the MEPE vanishes near the centre (Thais *et al.* 2013). Note that polymer chains absorb energy mainly from the MKE in the near-wall region, but from the TKE in the core region.

The energy production excess, defined as the TKE production P_m^+ over the dissipation ε, is plotted in pre-multiplied form in figure 11(*b*), so that equal areas underneath the curves correspond to equal integral contributions (Pirozzoli *et al.* 2014). The energy production excess has a Newtonian peak value at $y^+ \sim 10$ where the near-wall turbulence self-sustaining cycle is most energetic. It shifts away from the wall with the increase of *We* as a consequence of thickening of the buffer layer. Here, the most intriguing change of the energy production excess occurs in the core region. Specifically, a significant increase from a Newtonian negative value to a much higher positive value at $We = 7$ is observed. Together with the prominent energy absorption by polymer chains, this results in the great increase of TKE in the core region (see figure 5*d*).

5. Effects of large-scale structures

It has been found that LSSs have a great influence on Newtonian turbulent PCF (Komminaho *et al.* 1996; Tsukahara *et al.* 2006). However, their influence on drag-reduced viscoelastic flow is unknown. In what follows, our initial exploration into the effects of LSSs in drag-reduced PCF is discussed.

The imprint effects of LSSs on near-wall turbulence are clearly evidenced by the pre-multiplied energy spectra (see figure 12; the spectral density of $We = 2$ is not shown for the sake of brevity; it has no significant difference as compared to the Newtonian case), as well as the change in length scales of coherent structures in the near-wall region and LSSs in the core region (Kim & Adrian 1999; Guala *et al.* 2006; Tsukahara *et al.* 2006; Monty *et al.* 2009; Pirozzoli *et al.* 2014). For Newtonian PCF (see figure 12*a*), two energy-condensed zones can be seen in the near-wall region but only one can be seen in the core region. The energy-condensed zone centred at $\lambda_z^+ \sim 100$ represents the typical self-sustained coherent structures of spanwise wavelength of approximately 100 wall units in the buffer layer. This is similar to other canonical wall-bounded shear turbulence in the near-wall region (Monty *et al.* 2009). Even though *Re* in our calculation is relatively low compared to the recent study of Pirozzoli *et al.* (2014), the energy-condensed zone in the core region is still distinct due to the presence of LSSs. The imprint effect of LSSs is clearly evidenced by the secondary near-wall energy-condensed zone centred at about $\lambda_z^+ = 300$. This indicates that the LSSs have an average spanwise wavelength of approximately 300 wall units, corresponding to a wavenumber of $\sim 5/3$ in the spanwise direction. For other canonical wall-bounded turbulence such as PPF and turbulent boundary layer, this secondary near-wall energy-condensed zone appears only at a much higher *Re*. The imprint effects of LSSs help to explain why the spanwise scale of near-wall flows estimated by two-point correlations (see figure 2*a*) is approximately 120 as opposed to 100 in wall units. Specifically, the estimate based on two-point correlations yields a spanwise scale larger than that of near-wall small-scale coherent structures but smaller than that of LSSs.

The introduction of polymer additives into Newtonian PCF has a great influence on both coherent structures in the near-wall region and LSSs in the core region. As depicted in figures 12(*b*) and 12(*c*), the first energy-condensed zone corresponds to coherent structures centred at larger λ_z^+, i.e. $\lambda_z^+ = 148$ for $We = 5$ and $\lambda_z^+ = 158$ for $We = 7$. This change indicates that the increase in the spanwise scale of self-sustained

https://doi.org/10.1017/jfm.2018.242 Published online by Cambridge University Press

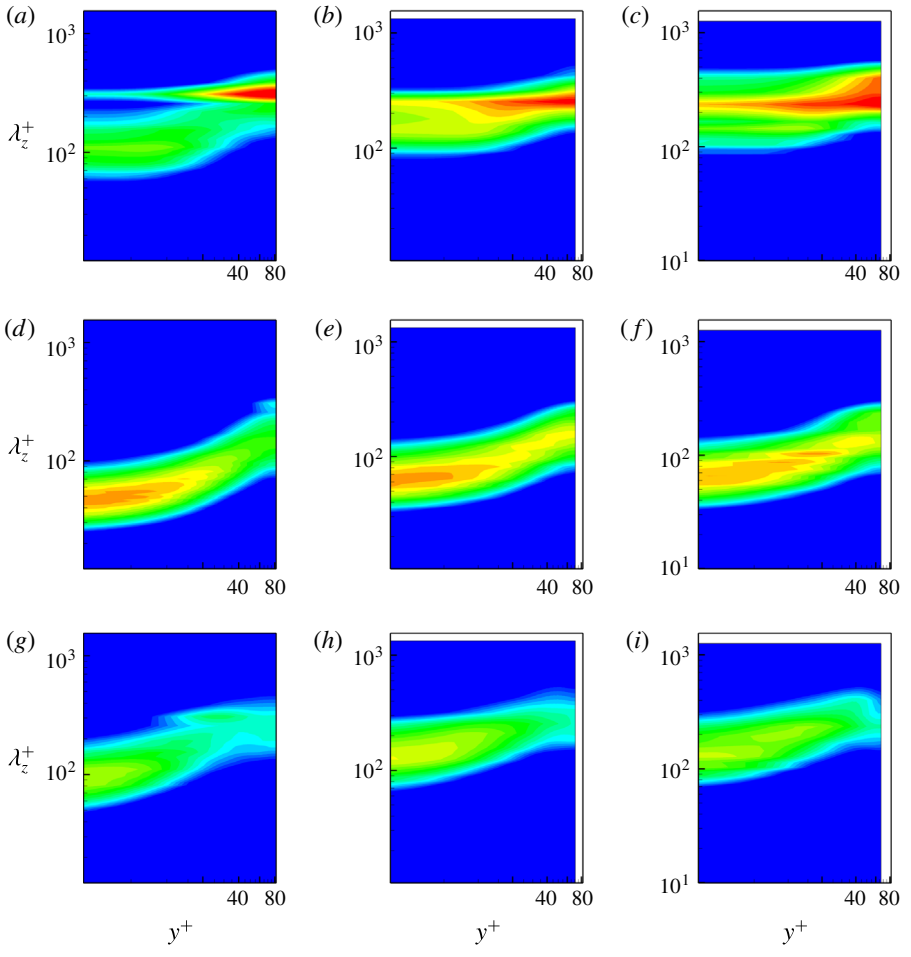


FIGURE 12. (Colour online) Pre-multiplied spanwise spectral density $k_zE(k_z)$ ($\int_0^\infty E_{u_iu_i}(k_z)\,\mathrm{d}k_z = \overline{u_i'^2}$) normalized by $\overline{u_i'^2}$ and varying with wall distance for Newtonian flow (*a*,*d*,*g*), $We = 5$ (*b*,*e*,*h*) and $We = 7$ (*c*,*f*,*i*). (*a–c*) k_zE_{uu}; (*d–f*) k_zE_{vv}; (*g–i*) k_zE_{ww}. Twenty contour levels are shown, from 0.16 to 0.4.

coherent structures in the buffer layer is due to the polymer addition. It has been noted that a formula proposed by (Tiederman 1990) and verified by Sureshkumar *et al.* (1997) can be used to link the streak spacing with the extent of drag reduction as $\lambda_z^+ = 1.9DR\,\% + 99.7$. Accordingly, drag reduction of 26 % for $We = 5$ and 34 % for $We = 7$, correspond to streak spacing of 149 and 164, respectively. These λ_z^+ values predicted by this formula are consistent with our simulation results. Moreover, this energy-condensed zone becomes wider in the wall-normal direction, indicating that the influence of the coherent structures in the buffer layer is enhanced by polymer addition and affects larger distances from the wall.

The change of the LSSs in the core region in response to the introduction of polymer additives is discussed below. Figure 12(*b*) shows that for $We = 5$, the energy-condensed zone in the core region is centred at $\lambda_z^+ \sim 260$; still corresponding to the wavenumber $\sim 5/3$ for LSSs in the spanwise direction. Thus, the spanwise scale of the LSSs stays unchanged. Moreover, the secondary near-wall energy-condensed

https://doi.org/10.1017/jfm.2018.242 Published online by Cambridge University Press

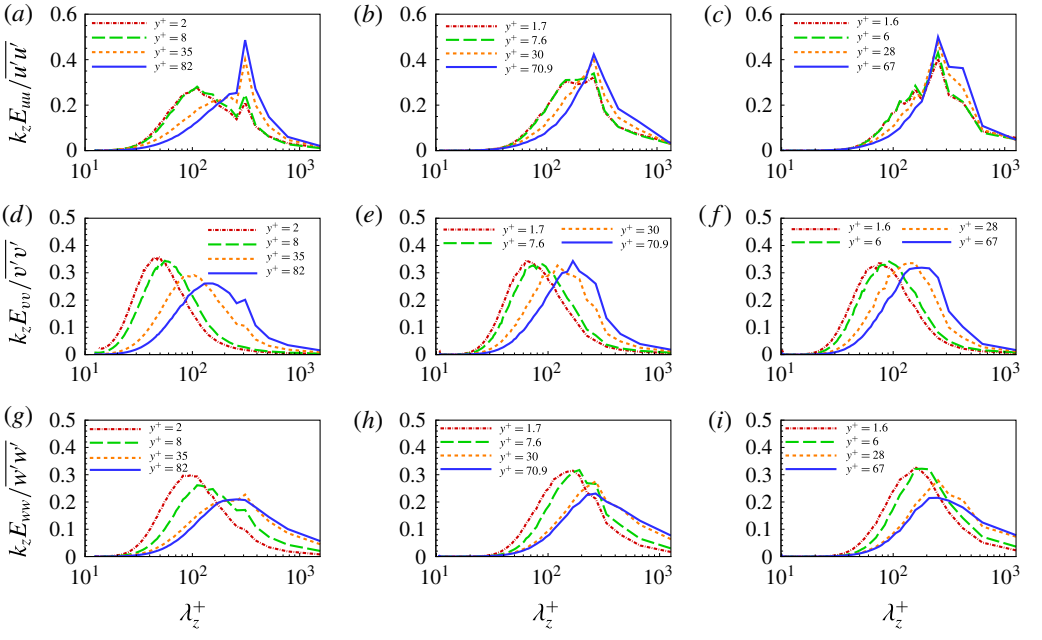


FIGURE 13. (Colour online) Pre-multiplied spanwise spectral density of velocity fluctuations at different wall distances for Newtonian flow (*a*,*d*,*g*), $We = 5$ (*b*,*e*,*h*) and $We = 7$ (*c*,*f*,*i*). (*a–c*) $K_z E_{uu}$; (*a–c*) $K_z E_{vv}$; (*a–c*) $K_z E_{ww}$.

zone has an enhanced contribution, which reflects that the LSSs have stronger imprint effects on the near-wall turbulence. When *We* increases further to 7, the core-region energy-condensed zone indicates that the LSSs have the same wavenumber, i.e. $\sim 5/3$ in the spanwise direction, while the imprint effects become more significant and penetrate the whole channel. Overall, figure 12(*a–c*) shows that the energy spectra in the near-wall region are dominated by coherent structures for Newtonian PCF, and the LSSs' contribution increases monotonically with increasing *We* for drag-reduced cases. However, at *We* of 7, the energy spectra of near-wall turbulence is dominated by imprint effects of LSSs.

Figure 13 presents the pre-multiplied energy spectra at different wall distances. In the near-wall region, two distinct peaks can be identified for the spectra of the streamwise velocity fluctuation. The first peak denotes the spanwise scale of self-sustained coherent structures; the second one corresponds to the imprint effects of LSSs. In the core region, only one peak occurs, which denotes the spanwise scale of LSSs. With the increase of *We*, the first near-wall peak of the spectra occurs at $\lambda_z^+ \sim 100$ for Newtonian PCF and it changes to $\lambda_z^+ \sim 148$ for $We = 5$ and $\lambda_z^+ \sim 158$ for $We = 7$. This quantitatively demonstrates that the coherent structures have a substantial increase in spanwise scale in the near-wall region. However, the second near-wall peak and the core-region peak of the spectra both correspond to the fact that the wavenumber in the spanwise direction is $\sim 5/3$, which remains unaltered with the increase of *We*. This is consistent with the estimate based on figure 12.

The influence of LSSs can be quantified by examining the relative contributions of different wavelengths to the total energy (or shear stress). The cumulative contributions

https://doi.org/10.1017/jfm.2018.242 Published online by Cambridge University Press

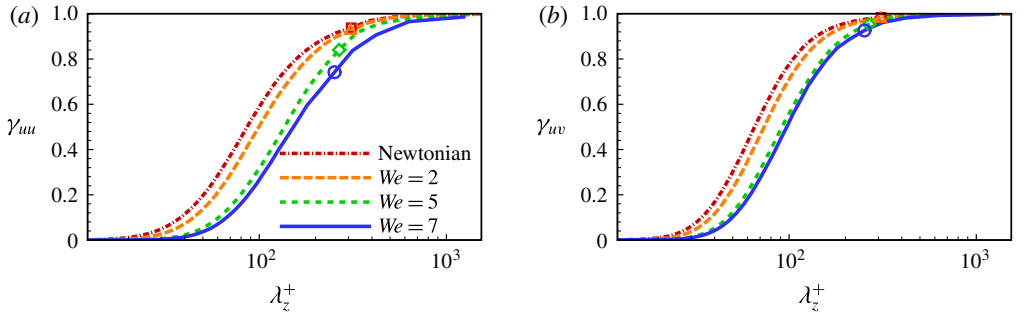


FIGURE 14. (Colour online) Cumulative fraction of the streamwise kinetic energy γ_{uu} (a) and of the Reynolds stress γ_{uv} (b) at $y^* = 0.1$ where y^* is the wall distance. The symbols in the plots represent the spanwise scales of LSSs for different calculations.

to $\overline{u_i' u_j'}$ are evaluated in spectral space as

$$\gamma_{ij}(k_z) = 1 - \frac{\sum_{0}^{k} E_{ij}(\tilde{k}_z)}{\sum_{0}^{k_{max}} E_{ij}(\tilde{k}_z)}, \tag{5.1}$$

where E_{ij} is the spectral density of $\overline{u_i' u_j'}$ (Guala *et al.* 2006; Balakumar & Adrian 2007). $\gamma_{ij}(k_z)$ denotes the relative contribution of large-scale motions with wavenumber $> k_z$. The cumulative contributions $\gamma_{uu}(k_z)$ and $\gamma_{uv}(k_z)$ have been calculated in the near-wall region (see figure 14). It is indicated that the relative contribution of large-scale motions substantially increases with the increase of *We*. Note that the spanwise scales of LSSs are denoted by symbols in the plots. From $\gamma_{uu}(k_z)$, the large scales ($\geqslant$ the spanwise scales of LSSs) have a cumulative contribution of 6 % for Newtonian PCF, which increases to 8 % for $We = 2$, then to 16 % for $We = 5$ and eventually to 26 % for $We = 7$. As for $\gamma_{uv}(k_z)$, a corresponding increase in cumulative contribution is found from 1.6 % to 2.1 %, then to 5 %, and eventually to 7 %. These two changes likely stem from the increasing imprint effects of LSSs on the near-wall flow.

The nonlinear effects of LSSs on the near-wall flows can be quantified by an amplitude modulation coefficient calculated using the Hilbert transform and a Fourier filter (Mathis *et al.* 2009). The modulation coefficient has a strong resemblance to the skewness profile of u' (Mathis *et al.* 2011). To this end, the skewness of u' is examined here to ascertain the effects of modulation on the LSSs. As shown in figure 15(a), the skewness increases monotonically with the increase of *We*, indicating an enhancement of the modulation effects of LSSs. Moreover, the increase of the skewness implies that the asymmetry of the streamwise fluctuations is enhanced. Also, the flatness increases monotonically with the increase of *We* (see figure 15b), which suggests a stronger intermittency of streamwise fluctuating motions (Pirozzoli *et al.* 2014). The increased near-wall intermittency has also been related to the modulation imparted by LSSs (Mathis *et al.* 2009) and is consistent with the explanation that drag reduction is commensurate with an increased interval of hibernating turbulence (Xi & Graham 2012). With the increase of *We*, the skewness and flatness of u' in the near-wall region demonstrate a clear deviation from the Gaussian behaviour,

https://doi.org/10.1017/jfm.2018.242 Published online by Cambridge University Press

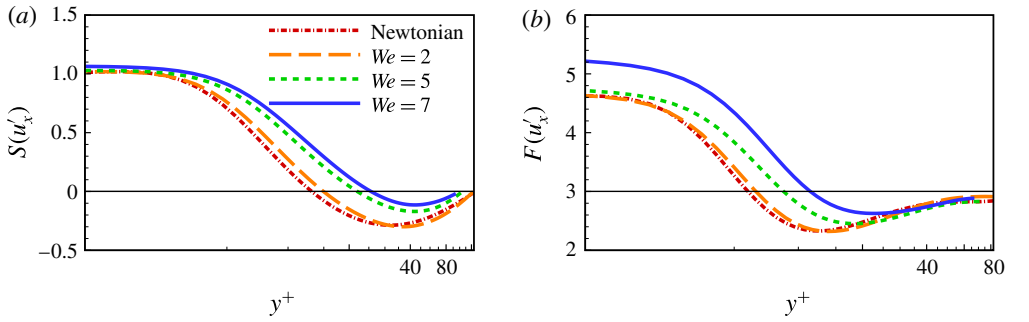


FIGURE 15. (Colour online) The skewness (*a*) and flatness (*b*) of the streamwise velocity fluctuation, defined as $S(u') \equiv \overline{u'^3}/(\overline{u'^2})^{3/2}$ and $F(u') \equiv \overline{u'^4}/(\overline{u'^2})^2$, respectively.

namely, $S(u') = 0$ and $F(u') = 3$, while at the channel centre they are close to the Gaussian values. This is very different from the findings of Samanta *et al.* (2009) in drag-reduced PPF especially in the core region.

The increasing effects of LSSs on the near-wall flow are further evidenced by the monotonic increase of the peak value of u'^+_{rms} shown in figure 5(*a*). According to previous studies (Marusic *et al.* 2010; Orlandi *et al.* 2015; Smits 2015), for Newtonian turbulence, the peak value of u'^+_{rms} should be invariant to the increase of Re if not affected by fluid flow above the buffer layer; however, the effects of core-region LSSs do indeed cause a deviation. Thus, the enhancement of u'^+_{rms} peak value due to the increase of We (see figure 5*a*) results from the increasing influence of the LSSs on near-wall turbulence. This is consistent with the above discussions which indicate that the imprint and modulation effects of LSSs are enhanced in drag-reduced PCF.

The roll cells appearing in PCF are reminiscent of the well-known Taylor vortices found in Taylor–Couette flow. However, the Taylor vortices and the roll cells discussed here are distinct, because the Taylor vortices are formed as a consequence of a centrifugal instability while the roll cells are formed due to a quasi-periodic process in which low-speed velocity streaks generate large-scale vortices (Hamilton *et al.* 1995). The roll cells can be visualized by streamline plots based on the velocity vector $(\boldsymbol{v}, \boldsymbol{w})$ averaged in time and in the streamwise direction (Komminaho *et al.* 1996; Avsarkisov *et al.* 2014; Niebling *et al.* 2014). In figure 16, the roll cells, composed of 5 pairs of counter-rotating vortices, are clearly visualized for Newtonian PCF and drag-reduced flows. Note that this number of roll cell pairs corresponds to a wavenumber of $\sim 5/3$ in the spanwise direction. These well-shaped structures can be obtained only by ensemble averaging based on a sufficiently large sample size of flow fields, especially at high Re. As shown in figure 16, the roll cells penetrate the entire channel and thus have a vertical scale of the channel height. Evidently, these roll cells should be treated as LSSs.

Next, we would like to recall some evidence that implies that the roll cells are the key LSSs in the core region. First, as predicted by $R_{uu}(\Delta z)$ in figure 2(*b*,*d*,*f*), the LSSs in the core region have a spanwise scale of approximately 3.70, corresponding to the number of roll cell pairs of $N = 6\pi/3.70 \approx 5$. This prediction agrees well with the number of roll cells observed in figure 16. These roll cell structures should be responsible for the minima of $R_{uu}(\Delta z)$ in the core region as observed in figure 2(*b*,*d*,*f*) (Avsarkisov *et al.* 2014). Second, in figures 12 and 13, the pre-multiplied spectra of the streamwise velocity fluctuation point to an estimate that the LSSs in the core

https://doi.org/10.1017/jfm.2018.242 Published online by Cambridge University Press

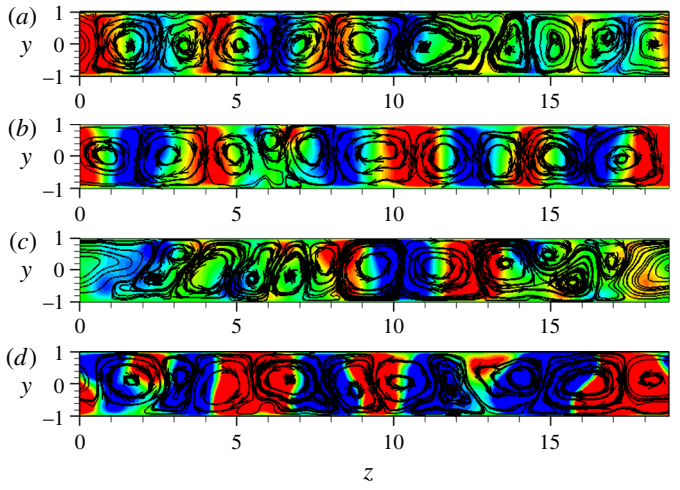


FIGURE 16. (Colour online) Large-scale structures (roll cells) visualized by streamline plots of the ensemble-averaged velocity vector $(\boldsymbol{v}, \boldsymbol{w})$ for Newtonian flow (a) and drag-reduced flows with $We = 2$ (b), $We = 5$ (c) and $We = 7$ (d) (Komminaho *et al.* 1996; Avsarkisov *et al.* 2014). The ensemble average is performed in time and streamwise directions. The contour denotes the value of streamwise velocity fluctuation. Twenty contours are plotted in $(-0.02, 0.02)$. Five pairs of roll cells can be seen in all the figures.

region have a wavenumber of $\sim 5/3$ in the spanwise direction. This estimate is also consistent with the number of roll cell pairs identified in figure 16. Moreover, it is shown in figure 16 that the number of roll cells stays basically the same for Newtonian and viscoelastic PCF. This feature is in good agreement with the above findings that the spanwise wavelength of LSSs remains unaltered for all the cases considered. Here, it is of special interest that the introduction of polymer additives has no influence on the spanwise scales of LSSs, namely, roll cells.

6. Conclusions

In this work, we have employed DNS to study drag reduction phenomena in PCF of dilute polymeric solutions. In particular, we have focused on exploring the similarities and differences in the drag reduction features of PCF and PPF and clarifying the effects of LSSs on the near-wall turbulence.

Specifically, we found that PCF has the typical drag reduction features of wall-bounded turbulence similar to those of PPF. The viscoelastic PCF considered obtains a drag reduction of $\sim 34\,\%$, an extent commonly assigned to the LDR regime. In the near-wall region, the scales of coherent structures are increased especially in the spanwise direction due to the polymer additives. With the increase of *We*, the polymer shear stress has an increasing contribution to the overall force balance commensurate with a monotonic decrease of the Reynolds shear stress. The log-law profile of mean streamwise velocity demonstrates a trend toward the well-known Virk asymptote. Similar to its counterpart, PPF, the streamwise velocity fluctuation of drag-reduced PCF is enhanced in the buffer layer and the core region; the other two components are suppressed with the increase of *We*. Moreover, the peak value of turbulent kinetic energy occurs at a larger wall distance due to the polymer additives, implying that the buffer layer shifts away from the wall. As indicated

https://doi.org/10.1017/jfm.2018.242 Published online by Cambridge University Press

by the variation of streamwise vorticity fluctuation, the quasi-streamwise vortices are greatly suppressed in the near-wall region, which in turn points to a suppressive effect of polymer additives on the self-sustaining process of near-wall turbulence. These drag reduction features are found in other wall-bounded drag-reduced flows, which is reasonable, since it is commonly held that the self-sustaining process in the near-wall region of wall-bounded turbulent flows is essentially the same. This in some sense supports the consensus that the self-sustained coherent structures are essentially the same for wall-bounded turbulence.

The distinct differences between drag-reduced PCF and PPF occur mainly in the core region, where LSSs, like roll cells, appear only in PCF. It is interesting to note that longitudinal streaks of large scales are identified at the channel centre and are enhanced greatly by polymer elasticity. Originating in the non-zero mean flow shear at the channel centre and the LSSs, polymer dynamics and budget balance in PCF are found to be strikingly different from those of PPF. Specifically, there is considerable polymer stretch in the core region as indicated by the distributions of mean conformation tensor components. Consequently, the energy budgets show that the polymer chains absorb substantial energy from turbulence in the core region. This energy absorption results in an increase of the production/dissipation ratio, which in turn accounts for the enhanced longitudinal streaks and turbulent kinetic energy in the core region. The energy transfer via polymer stretching also results in a large value of elastic potential energy in the core region of PCF; on the contrary, elastic potential energy is negligibly small (approaching zero) for drag-reduced PPF. According to the elastic theory, drag reduction in PPF stems from the energy transfer facilitated by polymer stretch. Specifically, the substantial exchange of elastic and turbulence energy found in the core region is an essential component of any effort aimed at understanding the mechanism of polymer-induced drag reduction, particularly in regards to the large flow structures that are observed in PCF.

Of great interest here are the imprint effects of LSSs on the near-wall turbulence in drag-reduced PCF, which can be seen by examining the pre-multiplied energy spectra. The imprint effects of LSSs on near-wall flow become enhanced with the increase of We, which accounts for the increase in peak value of the streamwise velocity fluctuations in the buffer layer. Moreover, the spanwise scales of LSSs are shown to be unchanged with the increase of We. In particular, the roll cells have 5 pairs corresponding to a wavenumber of $\sim 5/3$ in the spanwise direction, which is consistent with the estimate of the spanwise scale for LSSs.

In summary, our DNS results confirm that many drag-reduction-related features in PPF also exist in drag-reduced PCF. However, there are striking differences between PCF and PPF in the core region: specifically, the polymers pronouncedly absorb turbulent kinetic energy there. Furthermore, the polymer additives enhance the imprint effect of LSSs on near-wall flows, although the spanwise scale of the LSSs does not change.

Acknowledgements

This work is supported by the NSFC grants 11472268, 91752110, 11572312, and 11621202, the NSF grant CBET0755269 and Science Challenge Project (no. TZ2016001). This research is also supported in part by allocation of advanced computational resources on DARTER by the National Institute for Computational Sciences (NICS).

https://doi.org/10.1017/jfm.2018.242 Published online by Cambridge University Press

Appendix A

For MKE $K_m^+ = \overline{u_i u_i}^+/2$, TKE $K^+ = \overline{u_i' u_i'}^+/2$ and EPE $E_p^+ = (1/2)(1/We_\tau)(1-\beta/\beta)(L^2-3)\overline{\ln[f(\boldsymbol{C})]}$ (Dallas *et al.* 2010; Thais *et al.* 2013) with $We_\tau = \rho\lambda u_\tau^2/\eta_s$, the budget equations normalized with u_τ^4/ν are given respectively as (Thais *et al.* 2013)

$$\frac{DK_m^+}{Dt^+} = -P_m^+ - P_{pm}^+ - \varepsilon_m^+ + D_{m\nu}^+ - D_{mP}^+ - D_{mt}^+ + D_{pm}^+, \tag{A 1}$$

$$\frac{DK^+}{Dt^+} = P_m^+ - P_{pt}^+ - \varepsilon^+ + D_\nu^+ - D_P^+ - D_t^+ + D_{pt}^+, \tag{A 2}$$

and

$$\frac{DE_p^+}{Dt^+} = P_{pm}^+ + P_{pt}^+ - \varepsilon_{pm}^+ - \varepsilon_{pt}^+. \tag{A 3}$$

The definitions of the terms in the energy budget equations (A 1), (A 2) and (A 3) are given as:

$$\left.\begin{aligned}
&P_m^+ = -\tau_{ik}^+ \overline{S_{ki}}^+, \quad P_{pm}^+ = \overline{\tau_{ik}^p}^+ \overline{S_{ki}}^+, \quad \varepsilon_m^+ = \frac{\partial \overline{u_i}^+}{\partial x_k^+}\frac{\partial \overline{u_i}^+}{\partial x_k^+}, \quad D_{m\nu}^+ = \frac{\partial^2 K_m^+}{\partial x_k^+ \partial x_k^+},\\
&D_{mP}^+ = \frac{\partial(\overline{p}^+ \overline{u_i}^+)}{\partial x_i^+}, \quad D_{mt}^+ = \frac{\partial(\overline{u_i}^+ \tau_{ik}^+)}{\partial x_k^+}, \quad D_{pm}^+ = \frac{\partial \overline{u_i \tau_{ik}^p}^+}{\partial x_k^+}, \quad P_{pt}^+ = \overline{\tau_{ik}'^p}^+ \overline{S_{ki}'}^+,\\
&\varepsilon^+ = \overline{\frac{\partial u_i'}{\partial x_j}\frac{\partial u_i'}{\partial x_j}}^+, \quad D_\nu^+ = \frac{\partial^2 K^+}{\partial x_k^+ \partial x_k^+}, \quad D_P^+ = \frac{\partial \overline{p' u_k'}^+}{\partial x_k^+}, \quad D_t^+ = \frac{\partial(\overline{u_i' u_i' u_k'}^+/2)}{\partial x_k^+},\\
&D_{pt}^+ = \frac{\partial \overline{\tau_{ik}'^p u_i'}^+}{\partial x_k^+}, \quad \varepsilon_{pm}^+ = \frac{1}{2We_\tau}\overline{f(\boldsymbol{C})}\ \overline{\tau_{ii}^p}^+, \quad \varepsilon_{pt}^+ = \frac{1}{2We_\tau}\overline{f'(\boldsymbol{C})\tau_{ii}'^{p+}},
\end{aligned}\right\} \tag{A 4}$$

where $\tau_{ij}^+ = \overline{u_i' u_j'}^+$ is the turbulent stress and $\overline{S_{ij}}^+ = 1/2(\partial \overline{u_i}^+/\partial x_j^+ + \partial \overline{u_j}^+/\partial x_i^+)$ is the mean strain rate tensor.

REFERENCES

AVSARKISOV, V., HOYAS, S., OBERLACK, M. & GARCÍA-GALACHE, J. P. 2014 Turbulent plane Couette flow at moderately high Reynolds number. *J. Fluid Mech.* **751**, R1.

BALAKUMAR, B. J. & ADRIAN, R. J. 2007 Large- and very-large-scale motions in channel and boundary-layer flows. *Phil. Trans. R. Soc. Lond.* A **365**, 665–681.

BECH, K. H., TILLMARK, N., ALFREDSSON, P. H. & ANDERSSON, H. I. 1995 An investigation of turbulent plane Couette flow at low Reynolds numbers. *J. Fluid Mech.* **286**, 291–325.

BENZI, R., CHING, E. S. C., HORESH, N. & PROCACCIA, I. 2004 Theory of concentration dependence in drag reduction by polymers and of the maximum drag reduction asymptote. *Phys. Rev. Lett.* **92**, 078302.

BENZI, R., DE ANGELIS, E., LVOV, V. S. & PROCACCIA, I. 2005 Identification and calculation of the universal asymptote for drag reduction by polymers in wall bounded turbulence. *Phys. Rev. Lett.* **95**, 194502.

BENZI, R., DE ANGELIS, E., L'VOV, V. S., PROCACCIA, I. & TIBERKEVICH, V. 2006 Maximum drag reduction asymptotes and the cross-over to the Newtonian plug. *J. Fluid Mech.* **551**, 185–195.

https://doi.org/10.1017/jfm.2018.242 Published online by Cambridge University Press

BERNARDINI, M., PIROZZOLI, S. & ORLANDI, P. 2013 The effect of large-scale turbulent structures on particle dispersion in wall-bounded flows. *Intl J. Multiphase Flow* **51**, 55–64.

BIANCOFIORE, L., BRANDT, L. & ZAKI, T. A. 2017 Streak instability in viscoelastic Couette flow. *Phys. Rev. Fluids* **2**, 043304.

DALLAS, V., VASSILICOS, J. C. & HEWITT, G. F. 2010 Strong polymer-turbulence interactions in viscoelastic turbulent channel flow. *Phys. Rev.* E **82**, 066303.

DEBUSSCHERE, B. & RUTLAND, C. J. 2004 Turbulent scalar transport mechanisms in plane channel and Couette flows. *Intl J. Heat Mass Transfer* **47**, 1171–1781.

DIMITROPOULOS, C. D., SURESHKUMAR, R., BERIS, A. N. & HANDLER, R. A. 2001 Budgets of Reynolds stress, kinetic energy and streamwise enstrophy in viscoelastic turbulent channel flow. *Phys. Fluids* **13**, 1016–1027.

DUBIEF, Y., WHITE, C. M., TERRAPON, V. E., SHAQFEH, E. S. G., MOIN, P. & LELE, S. K. 2004 On the coherent drag-reducing and turbulence-enhancing behaviour of polymers in wall flows. *J. Fluid Mech.* **514**, 271–280.

GRAHAM, M. D. 2014 Drag reduction and the dynamics of turbulence in simple and complex fluids. *Phys. Fluids* **26**, 101301.

GUALA, M., HOMMEMA, S. E. & ADRIAN, R. J. 2006 Large-scale and very-large-scale motions in turbulent pipe flow. *J. Fluid Mech.* **554**, 521–542.

HAMILTON, J. M., KIM, J. & WALEFFE, F. 1995 Regeneration mechanisms of near-wall turbulence structures. *J. Fluid Mech.* **287**, 314–348.

HELLSTRÖM, L. H. O., MARUSIC, I. & SMITS, A. J. 2016 Self-similarity of the large-scale motions in turbulent pipe flow. *J. Fluid Mech.* **792**, R1.

HOSSEINIEBALAM, F., HASSANZADEH, S. & GHAFFARPASAND, O. 2014 Dispersion and deposition mechanisms of particles suspended in a turbulent plane Couette flow. *Appl. Math. Model.* **37**, 2417–2429.

HU, Z., MORFEY, C. L. & SANDHAM, N. D. 2003 Sound radiation in turbulent channel flows. *J. Fluid Mech.* **475**, 269–302.

HWANG, J., LEE, J., SUNG, H. J. & ZAKI, T. A. 2016 Inner-outer interactions of large-scale structures in turbulent channel flow. *J. Fluid Mech.* **790**, 128–157.

HWANG, Y. & COSSU, C. 2010 Self-sustained process at large scales in turbulent channel flow. *Phys. Rev. Lett.* **105**, 044505.

JIMÉNEZ, J. & HOYAS, S. 2008 Turbulent fluctuations above the buffer layer of wall-bounded flows. *J. Fluid Mech.* **611**, 215–236.

JIMÉNEZ, J. & MOIN, P. 1991 The minimal flow unit in near-wall turbulence. *J. Fluid Mech.* **225**, 213–240.

JOVANOVIĆ, M. R. & KUMAR, S. 2010 Transient growth without inertia. *Phys. Fluids* **22**, 023101.

KAWATA, T. & ALFREDSSON, P. H. 2016 Experiments in rotating plane Couette flow – momentum transport by coherent roll-cell structure and zero-absolute-vorticity state. *J. Fluid Mech.* **791**, 191–213.

KIM, J., MOIN, P. & MOSER, R. 1987 Turbulence statistics in fully developed channel flow at low Reynolds number. *J. Fluid Mech.* **177**, 133–166.

KIM, K. C. & ADRIAN, R. J. 1999 Very large-scale motion in the outer layer. *Phys. Fluids* **11**, 417–422.

KITOH, O., NAKABYASHI, K. & NISHIMURA, F. 2005 Experimental study on mean velocity and turbulence characteristics of plane Couette flow: low-Reynolds-number effects and large longitudinal vortical structure. *J. Fluid Mech.* **539**, 199–227.

KITOH, O. & UMEKI, M. 2008 Experimental study on large-scale streak structure in the core region of turbulent plane Couette flow. *Phys. Fluids* **20**, 025107.

KLINE, S. J., REYNOLDS, W. C., SCHRAUB, F. A. & RUNSTADLER, P. W. 1967 The structure of turbulent boundary layers. *J. Fluid Mech.* **30**, 741–773.

KOMMINAHO, J., LUNDBLADH, A. & JOHANSSON, A. V. 1996 Very large structures in plane turbulent Couette flow. *J. Fluid Mech.* **320**, 259–285.

LAM, K. & BANERJEE, S. 1992 On the condition of streak formation in a bounded turbulent flow. *Phys. Fluids* A **4**, 306.

https://doi.org/10.1017/jfm.2018.242 Published online by Cambridge University Press

LI, C.-F., SURESHKUMAR, R. & KHOMAMI, B. 2015 Simple framework for understanding the universality of the maximum drag reduction asymptote in turbulent flow of polymer solutions. *Phys. Rev.* E **92**, 043014.

LI, C.-F., SURESHKUMAR, R. & KHOMAMI, B. 2006 Influence of rheological parameters on polymer induced turbulent drag reduction. *J. Non-Newtonian Fluid Mech.* **140**, 23–40.

LIU, C.-H. 2003 Turbulent plane Couette flow and scalar transport at low Reynolds number. *Trans. ASME J. Heat Transfer* **125**, 988–998.

LIU, N. & KHOMAMI, B. 2013*a* Elastically induced turbulence in Taylor–Couette flow: direct numerical simulation and mechanistic insight. *J. Fluid Mech.* **737**, R4.

LIU, N. & KHOMAMI, B. 2013*b* Polymer-induced drag enhancement in turbulent Taylor–Couette flows: direct numerical simulations and mechanistic insight. *Phys. Rev. Lett.* **111**, 114501.

LUMLEY, J. L. 1969 Drag reduction by additives. *Annu. Rev. Fluid Mech.* **1**, 367–384.

L'VOV, V. S., POMYALOV, A., PROCACCIA, I. & TIBERKEVICH, V. 2004 Drag reduction by polymers in wall bounded turbulence. *Phys. Rev. Lett.* **92**, 244503.

MARUSIC, I., MATHIS, R. & HUTCHINS, N. 2010 Predictive model for wall-bounded turbulent flow. *Science* **329**, 193–196.

MATHIS, R., HUTCHINS, N. & MARUSIC, I. 2009 Large-scale amplitude modulation of the small-scale structures in turbulent boundary layers. *J. Fluid Mech.* **628**, 311–337.

MATHIS, R., MARUSIC, I., HUTCHINS, N. & SREENIVASAN, K. R. 2011 The relationship between the velocity skewness and the amplitude modulation of the small scale by the large scale in turbulent boundary layers. *Phys. Fluids* **23**, 121702.

MIN, T., CHOI, H. & YOO, J. Y. 2003*a* Maximum drag reduction in a turbulent channel flow by polymer additives. *J. Fluid Mech.* **492**, 91–100.

MIN, T., YOO, J. Y., CHOI, H. & JOSEPH, D. D. 2003*b* Drag reduction by polymer additives in a turbulent channel flow. *J. Fluid Mech.* **486**, 213–238.

MONTY, J. P., HUTCHINS, N., NG, H. C. H., MARUSIC, I. & CHONG, M. S. 2009 A comparison of turbulent pipe, channel and boundary layer flows. *J. Fluid Mech.* **632**, 431–442.

NGUYEN, M. Q., DELACHE, A., SIMOENS, S., BOS, W. J. T. & HAJEM, M. E. 2016 Small scale dynamics of isotropic viscoelastic turbulence. *Phys. Rev. Fluids* **1**, 083301.

NIEBLING, M. J., TALLAKSTAD, K. T., TOUSSAINT, R. & MÅLØY, K. J. 2014 Direct velocity measurement of a turbulent shear flow in a planar Couette cell. *Phys. Rev.* E **89**, 013026.

ORLANDI, P., BERNARDINI, M. & PIROZZOLI, S. 2015 Poiseuille and Couette flows in the transitional and fully turbulent regime. *J. Fluid Mech.* **770**, 424–441.

PAGE, J. & ZAKI, T. A. 2014 Streak evolution in viscoelastic couette flow. *J. Fluid Mech.* **742**, 520–551.

PAGE, J. & ZAKI, T. A. 2015 The dynamics of spanwise vorticity perturbations in homogeneous viscoelastic shear flow. *J. Fluid Mech.* **777**, 327–363.

PASINATO, H. D. 2011 Velocity and temperature dissimilarity in fully developed turbulent channel and plane Couette flows. *Intl J. Heat Fluid Flow* **32**, 11–25.

PEREIRA, A. S., MOMPEAN, G., THAIS, L. & SOARES, E. J. 2017*a* Transient aspects of drag reducing plane Couette flows. *J. Non-Newtonian Fluid Mech.* **241**, 60–69.

PEREIRA, A. S., MOMPEAN, G., THAIS, L., SOARES, E. J. & THOMPSON, R. L. 2017*b* Active and hibernating turbulence in drag-reducing plane Couette flows. *Phys. Rev. Fluids* **2**, 084605.

PEREIRA, A. S., MOMPEAN, G., THOMPSON, R. L. & SOARES, E. J. 2017*c* Elliptical, parabolic, and hyperbolic exchanges of energy in drag reducing plane Couette flows. *Phys. Fluids* **29**, 115106.

PIZORROLI, S., BERNARDINI, M. & ORLANDI, P. 2011 Large-scale motions and inner/outer layer interactions in turbulent Couette-Poiseuille flows. *J. Fluid Mech.* **680**, 534–563.

PIROZZOLI, S., BERNARDINI, M. & ORLANDI, P. 2014 Turbulence statistics in Couette flow at high Reynolds number. *J. Fluid Mech.* **758**, 327–343.

PROCACCIA, I., L'VOV, V. S. & BENZI, R. 2008 Colloquium: theory of drag reduction by polymers in wall-bounded turbulence. *Rev. Mod. Phys.* **80**, 225–247.

https://doi.org/10.1017/jfm.2018.242 Published online by Cambridge University Press

PTASINSKI, P. K., BOERSMA, B. J., NIEUWSTADT, F. T. M., HULSEN, M. A., VAN DEN BRULE, B. H. A. A. & HUNT, J. C. R. 2003 Turbulent channel flow near maximum drag reduction: simulations, experiments and mechanisms. *J. Fluid Mech.* **490**, 251–291.

RAWAT, S., COSSU, C., HWANG, Y. & RINCON, F. 2015 On the self-sustained nature of large-scale motions in turbulent Couette flow. *J. Fluid Mech.* **782**, 515–540.

SAMANTA, G., HOUSIADAS, K. D., HANDLER, R. A. & BERIS, A. N. 2009 Effects of viscoelasticity on the probability density functions in turbulent channel flow. *Phys. Fluids* **21**, 115106.

SMITS, A. J. 2015 Canonical wall-bounded flows: how do they differ? *J. Fluid Mech.* **774**, 1–4.

STONE, P. A., ROY, A., LARSON, R. G., WALEFFE, F. & GRAHAM, M. D. 2004 Polymer drag reduction in exact coherent structures of plane shear flow. *Phys. Fluids* **16**, 3470–3482.

STONE, P. A., WALEFFE, F. & GRAHAM, M. D. 2002 Toward a structural understanding of turbulent drag reduction: nonlinear coherent states in viscoelastic shear flows. *Phys. Rev. Lett.* **89**, 208301.

SURESHKUMAR, R., BERIS, A. N. & HANDLER, R. A. 1997 Direct numerical simulation of the turbulent channel flow of a polymer solution. *Phys. Fluids* **9**, 743–755.

TABOR, M. & DE GENNES, P. G. 1986 A cascade theory of drag reduction. *Europhys. Lett.* **2**, 519–522.

TENG, H., LIU, N., LU, X. & KHOMAMI, B. 2015 Direct numerical simulation of Taylor–Couette flow subjected to a radial temperature gradient. *Phys. Fluids* **27**, 125101.

THAIS, L., GATSKID, T. B. & MOMPEANA, G. 2012 Some dynamical features of the turbulent flow of a viscoelastic fluid for reduced drag. *J. Turbul.* **13**, 1–26.

THAIS, L., GATSKID, T. B. & MOMPEANA, G. 2013 Analysis of polymer drag reduction mechanisms from energy budgets. *Intl J. Heat Fluid Flow* **43**, 52–61.

TIEDERMAN, W. G. 1990 The effect of dilute polymer solutions on viscous drag and turbulence structure. In *Structure of Turbulence and Drag Reduction*, pp. 187–200. Springer.

TOMS, B. A. 1949 Some observations on the flow of linear polymer solutions through straight tubes at large Reynolds numbers. In *Proceedings of the 1st International Congress of Rheology, Vol. 2* (ed. J. M. Burgers), vol. 2, pp. 135–141. North Holland.

TSUKAHARA, T., ISHIGAMIA, T., YUB, B. & KAWAGUCHIA, Y. 2011 DNS study on viscoelastic effect in drag-reduced turbulent channel flow. *J. Turbul.* **12**, 1–25.

TSUKAHARA, T., KAWAMURA, H. & SHINGAI, K. 2006 DNS of turbulent Couette flow with emphasis on the large-scale structure in the core region. *J. Turbul.* **7**, 19.

VIRK, P. S. 1975 Drag reduction fundamentals. *AIChE J.* **21**, 625–656.

WALEFFE, F. 1997 On a self-sustaining process in shear flows. *Phys. Fluids* **9**, 883–900.

WHITE, C. M. & MUNGAL, M. G. 2008 Mechanics and prediction of turbulent drag reduction with polymer additives. *Annu. Rev. Fluid Mech.* **40**, 235–256.

WU, X., BALTZER, J. R. & ADRIAN, R. J. 2012 Direct numerical simulation of a $30R$ long turbulent pipe flow at $R^+ = 685$: large- and very large-scale motions. *J. Fluid Mech.* **698**, 235–281.

XI, L. & GRAHAM, M. D. 2012 Intermittent dynamics of turbulence hibernation in Newtonian and viscoelastic minimal channel flows. *J. Fluid Mech.* **693**, 433–472.

https://doi.org/10.1017/jfm.2018.242 Published online by Cambridge University Press